Can neck fractures in proximal humeri be predicted by CT-based FEA?

Gal Dahan[a], Ori Safran[b], Zohar Yosibash[a,*]

[a] *School of Mechanical Engineering, The Iby and Aladar Fleischman Faculty of Engineering, Tel-Aviv University, Ramat-Aviv, Israel*
[b] *Department of Orthopaedics, Hadassah University Hospital, Jerusalem, Israel*

Abstract

Background: Proximal humeri fractures at anatomical and surgical neck ($\sim$ 5% and $\sim$50% incidence respectively) are frequent in elderly population. Yet, neither in-vitro experiments nor CT-based finite element analyses (CTFEA) have investigated these in depth. Herein we enhance Dahan et al *Clin. Biomech.*, 2019 (addressing anatomical neck fractures) by more experiments and specimens, accounting for surgical neck fractures and explore CTFEA's prediction of humeri mechanical response and yield force.

Methods: Four fresh frozen human humeri were tested in a new experimental configuration inducing surgical neck fractures. Digital image correlation (DIC) provided strains and displacements on humeri surfaces and used to validate CTFEA predictions. CTFEAs were enhanced herein to improve the accuracy at the proximal neck: A cortical bone mapping (CBM) algorithm was implemented to overcome insufficient scanning resolution, and a new trabecular material mapping was investigated.

Results: The new experimental setting induced impacted surgical neck fractures in all humeri. Excellent DIC to CTFEA correlation in strains was obtained at the shaft (slope 0.984, $R^2 = 0.99$) and a fair agreement (slope 0.807, $R^2 = 0.73$) at the neck. CBM algorithm had worsened the correlation, whereas the new material mapping had a negligible influence. Yield loads predictions improved considerably when trabecular yielding (maximum principal strain criterion) was considered instead of surface cortical yielding.

*Corresponding author
Email address: `yosibash@tauex.tau.ac.il` (Zohar Yosibash)

Discussion: CTFEA well predicts strains on the shaft and reasonably well on the neck. This enhances former conclusions by past studies conducted using SGs , now also evident by DIC. Yield load prediction for surgical neck fractures (involving crushing of trabecular bone) is predicted better by trabecular failure laws rather than cortex ones. Further FEA studies using trabecular orthotropic constitutive models and failure laws are warrant.

Keywords: Humerus, FEMs, Surgical neck fracture, Digital image correlation, Cortical bone mapping

1. Introduction

Finite element (FE) models based on quantitative computed tomography (QCT) scans are becoming a standard in biomechanics studies, and in particular for computing long bones stiffness and strength [24, 34, 37, 20, 8]. Specifically, the ability to compute bone's strength may be used to predict risk of fracture in different patients, thereby "grading" their need for preventive treatment. To achieve this goal and enable a reliable prediction of fracture initiation, models' validation must involve in-vitro experiments that could induce clinical/physiological fractures. We focus on the proximal humerus, which is the 3^{rd} most common site of osteoporotic fractures [7, 25, 41]. Only a limited number of studies considering destructive experiments on human humeri can be found [36, 11]. To the best of our knowledge, our previous study [8] is the only one to present in-vitro experiments resulting in physiological fractures in the proximal humerus obtained by well-defined boundary conditions (BCs). While in [8] anatomical neck fractures were considered, the current study addresses fractures in the surgical neck. Impacted surgical neck fracture is common in the elderly population, usually occurs when one falls on an out-stretched arm, causing fracture of the shaft at the surgical neck (located beneath the greater and lesser tuberosities) and its penetration into the head. It is the most frequent proximal humerus fracture, accounting for up to 50% of humeral fractures, yet no procedure that would in-vitro replicate this fracture is documented.

Several studies have recently reported relatively large differences (comparing experimental and FE strains) in the neck and head regions of long bones [8, 13, 19]. As opposed to the bone's shaft, having a smooth cylindrical geometry and a thick cortex, the neck/head regions are mostly characterized by a complex geometry and a thin cortical shell surrounding trabecular bone tissue. Inaccurate modeling of these features in the FE analysis may be the cause for the poor agreement with experiments usually obtained in these regions. In particular, we address uncertainty in the Young modulus - ash density relationship ($E(\rho)$) for a range of trabecular bone densities, resulting from two different empirical relationships [22, 23] that do not intersect; and clinical CT scanner resolution which is insufficient for scanning thin cortices [16, 2, 31, 32]. Several recent studies have dealt with correction of cortical thickness and density estimates from QCT scans using image processing tools and deconvolution approaches [29, 6, 9, 35, 18]. Most papers address the femoral neck, while the work done by [9] focused on human vertebras. We found no application of such models to the human humeri. Among the different studies, only those by [35, 18] also present application to FE models (of femurs), showing improvement in model predictions capabilities after applying the CBM deconvolution algorithm proposed by [39, 40, 38]. We herein implement this CBM algorithm, assessing whether it can overcome the scan artifacts for humeri as well.

In the current paper we introduce a new experimental set-up to create surgical neck fractures, while monitoring both strains and displacements by digital image correlation (DIC). We hypothesize that an experimental set-up constraining the humeral head is necessary for obtaining a fracture in the surgical neck. Experimental measurements, and in particular the yield force are used to validate QCT-based FE analyses (CTFEAs). Since surgical neck fractures are characterized by crushing the trabecular tissue by the shaft, we question whether the maximum principal strain on the cortex is the proper yield criterion when using CTFEAs to predict the experimental observations.

2. Methods

Four fresh-frozen human humeri (2 pairs, right and left , denoted FFH5R & L and FFH6R & L from female donors) kept frozen at -80°C were used for experiments. Humeri were obtained from the National Disease Research Interchange, Philadelphia, PA, USA and approval for study was granted by the local ethics committee. FFH5/6 are from 80/59 years-old, 167/170 cm height, 97/69 kg (cause of death stroke/cardiac arrest).

Humeri were defrosted at day of experiment, cleaned of soft tissue, cut 260 mm below top of the humeral head and mounted into a steel cylinder using PMMA (Figure 1 left). The steel cylinders are welded to square metal bases to enable registration of the QCT-based models to the experimental system axes. Each humerus was placed in a water container along with five K_2HPO_4 calibration solutions (concentrations: 0 to 300 mg/cc [27]) and CT scanned using a Brilliance 64 scanner (Philips Healthcare, Eindhoven, The Netherlands). Scanning parameters were 120 kVp, exposure of 250 mAs, slice thickness 1 mm (equal to slice spacing), and pixel sizes of 0.2021, 0.207 and 0.2148 mm for FFH5 (R&L), FFH6L & FFH6R respectively.

Bones were painted by white with black speckles for DIC imaging (matte spray paints). For reference measurements 4-6 strain-gauges (SGs) (C2A-06-125LW-350, Micro-Measurements, NC, USA) were bonded to bones' surface prior to painting, at locations shown in Figure 1 right.

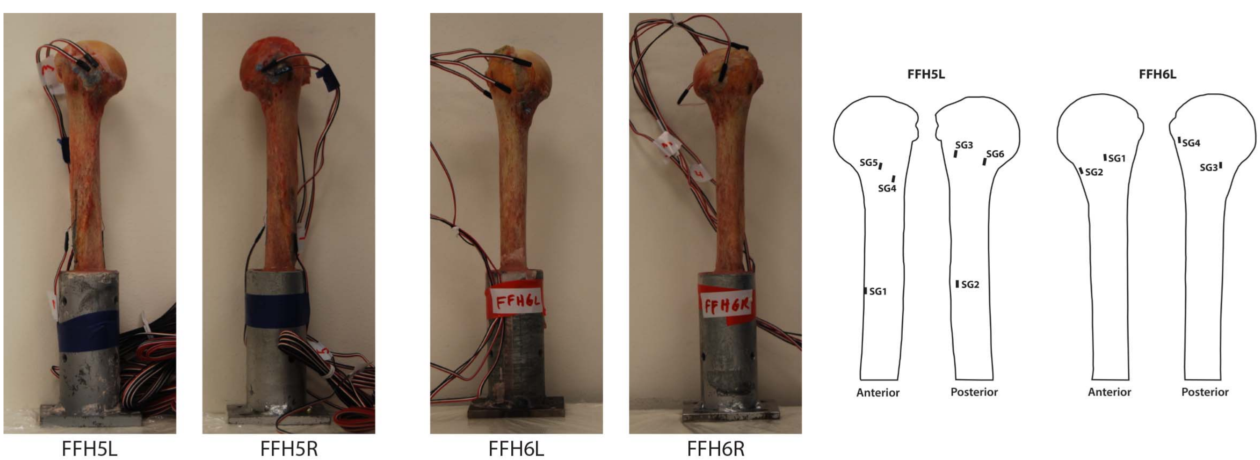

Figure 1: Left: The 4 humeri tested in the experiments, Right: Strain gauges locations showed on left humerus for each pair (locations were correspondingly located on right bones).

Prior to destructive experiments, humeri were loaded in elastic phase. Two loading configurations (denoted as *25* and *frac*) were used, loads directions are defined using α and β angles in a coordinate system on the humeral head, as detailed in [8]. The *25* boundary condition was chosen to simulate daily physiological loading on the humerus ($\alpha = 26.4^\circ$ and $\beta = 20^\circ$, based on [5]). Humeri distal end was mounted to the testing machine with load applied through their head by a flat plate. In *frac* configuration, designed to induce a fracture at bones' surgical neck, humeri were fixed to the testing machine with proximal part pointing downwards, humeral head immersed in PMMA ($\alpha = \beta = 0^\circ$) up to the proximal point of the lesser tuberosity. This mounting was designed to support the humerus head (as supported in-vivo by the muscles) and ensures fracture at the surgical neck.

In each experiment, two DIC systems (Correlated Solutions Inc., SC, USA) were placed on opposite sides of the humerus, in setting A, B or C (shown in Fig. 2 left). Each system consisted of two cameras (Grasshopper3 5MP, FLIR Systems Inc., OR, USA) with 35mm lenses (Xenoplan 1.9/35mm, Schneider Optics Inc., Bad Kreuznach, Germany), and two led spotlights. Polarizers were used to reduce glare. FFH5R and FFH5L were loaded at both *25* and *frac* configurations, imaged by settings A and B respectively. FFH6R and FFH6L were loaded only at *frac* configuration but in two repetitions, one imaged by setting B and the other by setting C. An example of a DIC test setting is shown in Fig. 2 right.

Each DIC system was positioned to capture an area of interest (AOI) as planar as possible on bone's surface. Cameras were located symmetrically about the AOI and in small stereo angles ($7^\circ - 15^\circ$) to obtain overlap of the visible fields. For uniform focus across the image, cameras' principal axis was placed perpendicular to the imaged surface. Once the cameras were positioned and aperture, exposure time and focus were adjusted, the humerus was removed and calibration was performed without moving the cameras setting. Calibration score of less than 0.05 pixels was obtained in all cases.

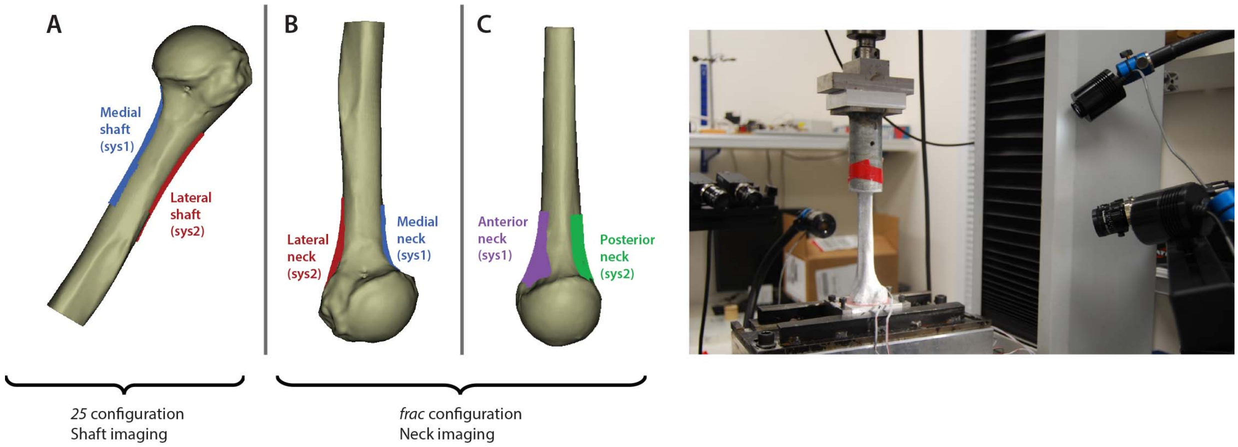

Figure 2: Left: DIC imaging settings used in the experiments. Setting A was used in the *25* configuration and settings B and C in the *frac* configuration. Right: Example of a DIC experimental set-up, imaging medial and lateral neck (setting B) in *frac* configuration.

Displacement control loading was applied using an AG-IC, Shimadzu machine (Kyoto, Japan). In the first loading (*25* configuration for FFH5R & L and first repetition of the *frac* configuration for FFH6R & L), humeri were loaded to 600 N in the vertical direction. In the second loading, at *frac* configuration for all humeri, load was applied until fracture. Forces were measured using a 6-axis load-cell (Omega191 F/T sensor, ATI Industrial Automation, NC, USA). SGs strains and forces were recorded by a Vishay 7000 data acquisition system (Micro-Measurements). DIC images were recorded by VicSnap software (Correlated Solutions Inc.), analog data was synchronized with DIC data using a multifunction I/O device (USB-6212, National Instruments Corp., TX, USA).

2.1. DIC post-processing

DIC images were processed by Vic-3D software (Correlated Solutions Inc.) to obtain displacement and strain fields . AOI for DIC analysis was defined in reference (first) image, the subset (facet) size was chosen such that subset correlation function's uncertainty interval (estimated σ) equals ~ 0.01 pixel, step size was set to ~ 0.25 of the subset size (manufacturer's recommendation). To prevent the subset size from being too large , the chosen AOI excluded areas that could bias the correlation (e.g. out-of-focus regions). Resulted subset sizes for the different AOIs in the different humeri were between 27 to 41 pixels (in each direction), and in average 0.9-1.6 mm (due to specimen curvature and cameras magnification the mm to pixel ratio in not uniform throughout the AOI). Strains were derived at each data point (located in the center of a subset and separated by the step size), calculated based on the displacements of four neighboring points. A spatial Gaussian decay filter (90% center-weighted) was applied to DIC strain fields to reduce noise, time filtering was also applied using a cubic spline. Since random errors characterizing the strains are enhanced in the AOI boundaries [10, 14, 19], and local errors are present at the edges even after smoothing, a 2 mm wide frame was removed from all DIC strain fields. To obtain an estimate of strain noise, static images (taken before load application) were analyzed. Any strain "measured" when the specimen was unloaded was assumed to be a result of random noise.

2.2. FE models

FE models of the four humeri were constructed using QCT data. Model geometry was obtained according to methods detailed in [42, 44]. Briefly, at each QCT slice the humerus boundary was detected based on a constant predefined threshold. Boundaries were thereafter smoothed to generate an outer geometry point cloud. A computer-aided design (CAD) model was then generated in Solidworks (Dassault Systèmes, Waltham, MA, USA) and imported to Abaqus (trademark of Dassault Systèmes). To allow an accurate simulation of the experimental setting, the QCT slices containing the mounting jigs (cylinder and square base) were also segmented and their CAD models were generated, then used to align the bone CAD model with the experimental system. HU values of voxels within the boundaries were used to generate the material properties file. The values were corrected at the boundaries to account for CT artifacts and then smoothed using a moving average algorithm [44, 21]. Each voxel's HU value was converted to equivalent mineral density ($\rho_{K_2HPO_4}$). $\rho_{K_2HPO_4}$ was converted to ash density using (1) [12] and (2) [33] and thereafter to Young's modulus, using relationships proposed by [23, 22] and given in (3 - 5).

$$\rho_{hydroxyapatite}\ [gr/cc] = 1.15 \times \rho_{K_2HPO_4} \tag{1}$$

$$\rho_{ash}\ [gr/cc] = 0.877 \times \rho_{hydroxyapatite} + 0.08 \tag{2}$$

$$E_{cort-Keller} = \quad 10200 \cdot \rho_{ash}^{2.01} \; [MPa] \;\; , \;\; \rho_{ash} > 0.486 \qquad [gr/cc] \tag{3}$$

$$E_{trab-const.} = \quad 2398 \; [MPa] \;\; , \;\; 0.3 < \rho_{ash} \leq 0.486 \qquad [gr/cc] \tag{4}$$

$$E_{trab-Keyak} = \quad 33900 \cdot \rho_{ash}^{2.2} \; [MPa] \;\; , \;\; \rho_{ash} \leq 0.3 \qquad [gr/cc] \tag{5}$$

The FE models were auto-meshed by 10-noded tetrahedral elements (300,000-350,000), resulting in $\sim$ 1.3-1.5 million DOFs. Loads and displacements were applied to mimic the experimental BC (Figure 3). For *25* loading, models were fixed at bone's distal face ($\vec{u} = 0$) and loaded through a 10 mm circular surface on the head ($F_Z = 600$ N and F_X,F_Y according to the forces measured in the specific experiment; XYZ being the coordinate system of the testing machine, Z being vertical direction). For *frac* loading, humeral head was fixed (whole part immersed in PMMA during experiment), and the distal face was subjected to a vertical displacement u_Z ($u_X = u_Y = 0$) resulting in a vertical load of 600 N.

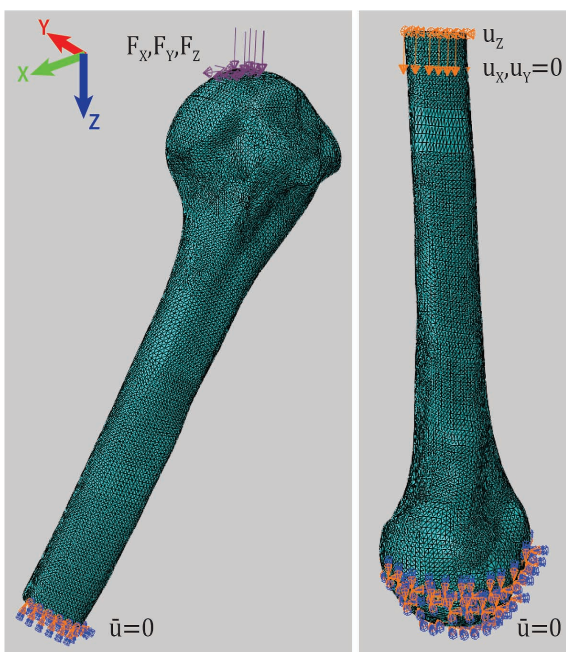

Figure 3: FE boundary conditions for the *25* (left) and *frac* (right) loadings. XYZ is the coordinate system of the testing machine.

2.2.1. Neck modeling

To overcome insufficient scanning resolution for thin cortices, the cortical bone mapping (CBM) algorithm, documented in [39, 40, 38], was implemented (public domain software Stradview v6.04, University of Cambridge, UK). Each humerus was re-segmented using Stradview, thereafter analyzed using the CBM algorithm, resulting in output files of cortical thickness and *corrected* HU values (after correction of CT artifacts), given at points on the bone's outer surface. Using to the cortical thickness output file, the nodes file (exported from the FE software) was divided into two groups (cortical and trabecular). All cortical nodes were assigned with the corrected HU value. The HUs were converted into Young's Modulus by Eqs. 1 - 5.

To determine the effect of $E(\rho)$ relationship for trabecular bone on strains in the neck, we considered a different relationship for the gap between [22] and [23] relationship. Comparing to the original relations (3-5) following changes were made: trabecular bone relationship was for densities lower than 0.2 g/cc (instead of 0.3 g/cc), cortical bone relationship was for densities higher than 0.7 g/cc (instead of 0.486 g/cc), and a linear interpolation relationship was for densities between 0.2-0.7 g/cc (instead of a constant value). New relations (changes in bold face) are given in (6-8).

$$E_{cort-Keller} = 10200 \cdot \rho_{ash}^{2.01} \; [MPa] \; , \; \boldsymbol{\rho_{ash} \geq 0.7}[gr/cc] \tag{6}$$

$$E_{cort-Keller} = \mathbf{7994.8 \cdot \boldsymbol{\rho_{ash}} - 616.2} \; [MPa] \; , \; \mathbf{0.2 < \boldsymbol{\rho_{ash}} \leq 0.7}[gr/cc] \tag{7}$$

$$E_{trab-Keyak} = 33900 \cdot \rho_{ash}^{2.2} \; [MPa] \; , \; \boldsymbol{\rho_{ash} \leq 0.2}[gr/cc] \tag{8}$$

2.3. Analysis of results

2.3.1. DIC vs SGs strains

We compared strains reported by DIC to SGs measurements by locating SGs in the DIC image. DIC strain in SG locations was averaged along an area similar to SG's measurement grid. The direction of the SG was in most cases aligned with the principal direction, thus principal strain reported by DIC was compared to SG data. In case the principal strain was not aligned with the SG, the relevant DIC strain component was computed and compared.Both DIC and SG strains were plotted as a function of force during loading, thereby evaluating their agreement. Strains at 600 N load were compared and their relative difference computed.

2.3.2. *CTFEA validation*

DIC measurements were compared to CTFEA predictions by registering DIC data to CAD (FE) coordinate system. Pair of closest points were located and principal strain values (compression in the neck, compression and tension in the shaft) were compared using Bland Altman [1] and robust linear regression plots. Mean absolute percentage error ($\%\bar{e}_{rel}$), root mean square error (RMSE) and RMSE divided by average strain (%RMSE) are reported. The *frac* loading configuration (with head immersed in PMMA) was simulated in the FE analysis by clamping the humeral head. DIC displacements were used to validate whether these boundary conditions represents the experiment correctly. Comparing DIC and CTFEA displacement fields requires a uniform reference point. Since the fixed surface of bones (the head) was not included in the DIC (and thus in matching FE field), a FE point having minimal vertical displacement ($\min(w)$) was defined as reference, and its displacement was subtracted from CTFEA displacement array. The corresponding (closest) point in the DIC field was found and same procedure applied.

2.3.3. *Yield loads*

CTFEA predicted yield loads and fracture initiation locations were compared to experimental observations. FE yield load was computed using maximum principal strain criterion [34, 43]. Maximum principal compression strain (ϵ_3) was identified in the FEA (ignoring local numerical errors), and averaged over a circular surface of a radius r=5 mm, considering values within 80% of the maximal strain. The load at which a critical principal strain value was obtained was calculated using linear extrapolation. Experimental yield load was defined as in [43, 8], according to the deviation from the linear force-strain curve in the DIC field closest to fracture.

The yield (critical) strains in compression ([3] and [17], for trabecular and cortical bone respectively) are shown in (9), the locations of the CTFEA predicted maximum strain were determined.

$$\begin{aligned} \varepsilon_{y-trab} &= \ -10400\ \mu strain \\ \varepsilon_{y-cort} &= \ -8600\ \mu strain \end{aligned} \tag{9}$$

3. Results

Thirteen DIC fields were analyzed, three were excluded (FFH5L setting B system 2, FFH6L setting C system 2, and FFH6R setting C system 1) due to glare in the images probably because of wet surfaces on the bones. DIC strains smoothed on 5 and 10 mm diameters were compared, showing differences in order of several tens of μstrains, and smaller than $\sim$ 9%. Such differences seem acceptable, suggesting that the filter size does not effect the results considerably. A filter size equivalent to a diameter of 10 mm was chosen, since it treats the boundary errors better.

DIC strains were compared to SGs measurements showing differences of at most $\sim$5% on the humeral shaft, and $\sim$ 10% on the neck. Based on the static images analyses, noise in the strain fields is of an order of several tens of μstrains.

3.1. FE boundary conditions validation

u_Z displacement (vertical direction of the testing machine) measured by DIC for the 4 humeri and the corresponding FEA fields are presented in Figure 4. In all figures the proximal part of the bone (where the displacement is minimal) is facing downwards. In some cases, considerable differences between the displacements fields can be observed, a phenomenon which is most severe at the medial and anterior neck of FFH6L and at the lateral neck of FFH5R and FFH6R. This outcome suggests that the humeral head was not fully fixed in these testings, making the BCs applied in the analyses inaccurate. Since for FFH6L, two out of three AOIs present an overall trend which is considerably different (comparing experiment to FE), it seems that clamping of the head in the FE model does not well represent the FFH6L experiment (a further thorough investigation showed air bubbles in the bone-PMMA interface), and thus this model was discarded. Strain validation was performed for the other three humeri, as detailed in the next section.

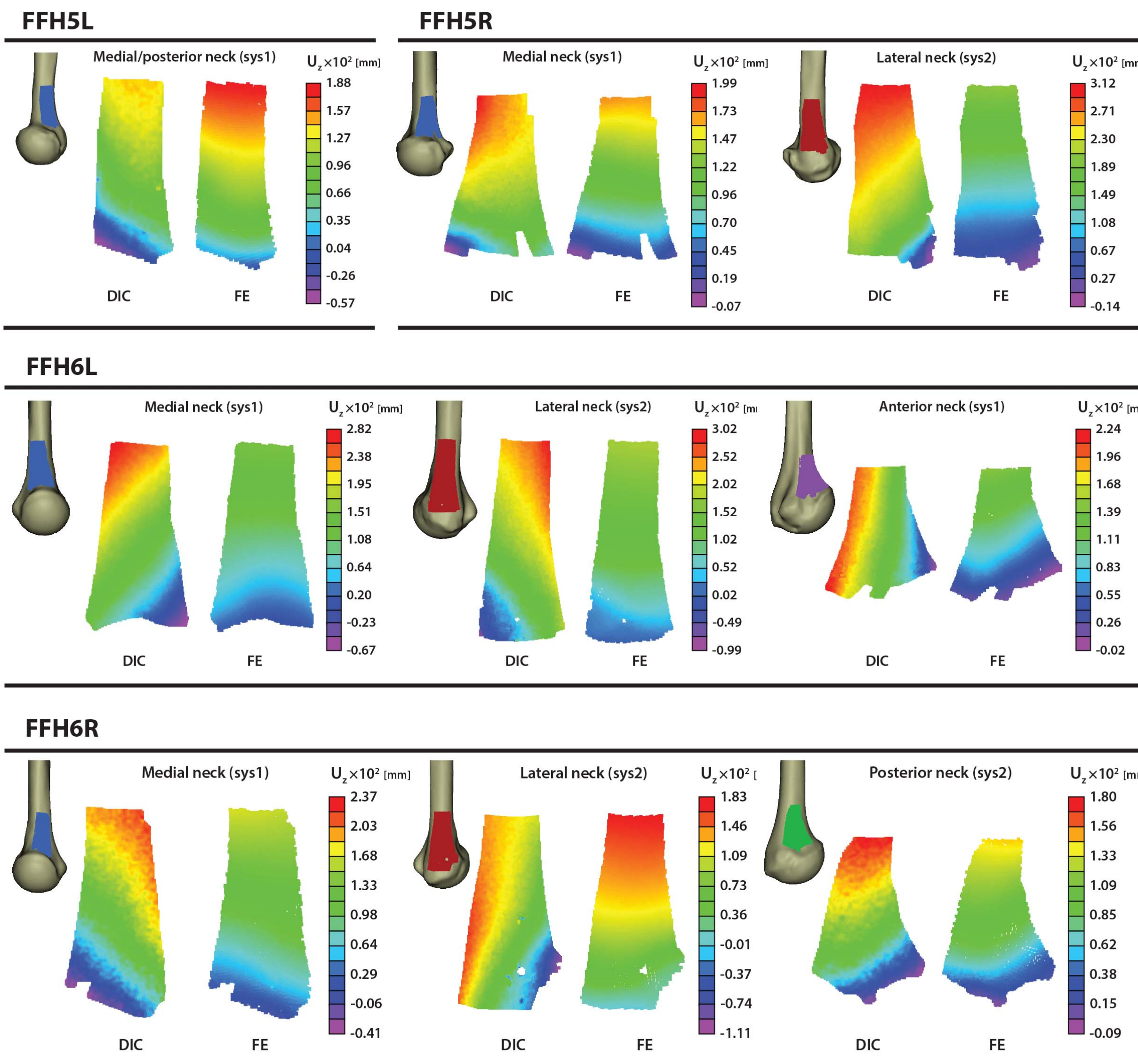

Figure 4: DIC vs FE vertical displacement for in the humeral neck of FFH5L, FFH5R, FFH6L and FFH6R. Values are in hundredth of a millimeter (1/100 mm).

3.2. FE strain validation

3.2.1. 25 loading configuration

Principal tensile strains (ϵ_1) in the medial shaft and principal compression strains (ϵ_3) in the lateral shaft for FFH5L and FFH5R, and the resulted linear regression and Bland Altman plots are presented in Figure 5. A small positive bias is indicated from the Bland-Altman plot (25 μstrain) implying slightly higher strains in the experiments. The mean absolute percentage error is 11.4 %, RMSE is 112 μstrain and %RMSE is 9.7 %. The linear regression for FFH5 humeri shaft strains is:

$$FE = 0.984 \times EXP - 44 \ , \ \ R^2 = 0.99 \tag{10}$$

The statistics for each bone separately are shown in Table 1.

3.2.2. Frac loading configuration

Principal compression strains in the medial, lateral or posterior neck for FFH5L, FFH5R and FFH6R are presented in Figure 6. Linear regression and Bland Altman plots showing agreement for neck strains in all 3 humeri is also presented. Resulted bias is almost zero (-8 μstrain), the mean absolute percentage error is 15 %, RMSE is 66 μstrain and %RMSE is 18.1 %. The linear correlation obtained in the neck strains is:

$$FE = 0.807 \times EXP - 69 \ , \ \ R^2 = 0.73 \tag{11}$$

The statistics for each bone separately are shown in Table 1.

Table 1: Agreement statistics obtained for the different humeri, for both shaft and neck regions.

Region	Bone	Slope	Intercept [μstrain]	R^2	RMSE [μstrain]	%RMSE	$\%\bar{e}_{rel}$
Shaft	FFH5L	0.977	-70.8	0.994	127	10.1	11.5
	FFH5R	0.994	-21.3	0.994	97	9	11.2
Neck	FFH5L	0.736	-86.5	0.782	70	17	15
	FFH5R	0.628	-146	0.628	71	18.4	15.7
	FFH6R	0.853	-35.1	0.765	60	18	15.4

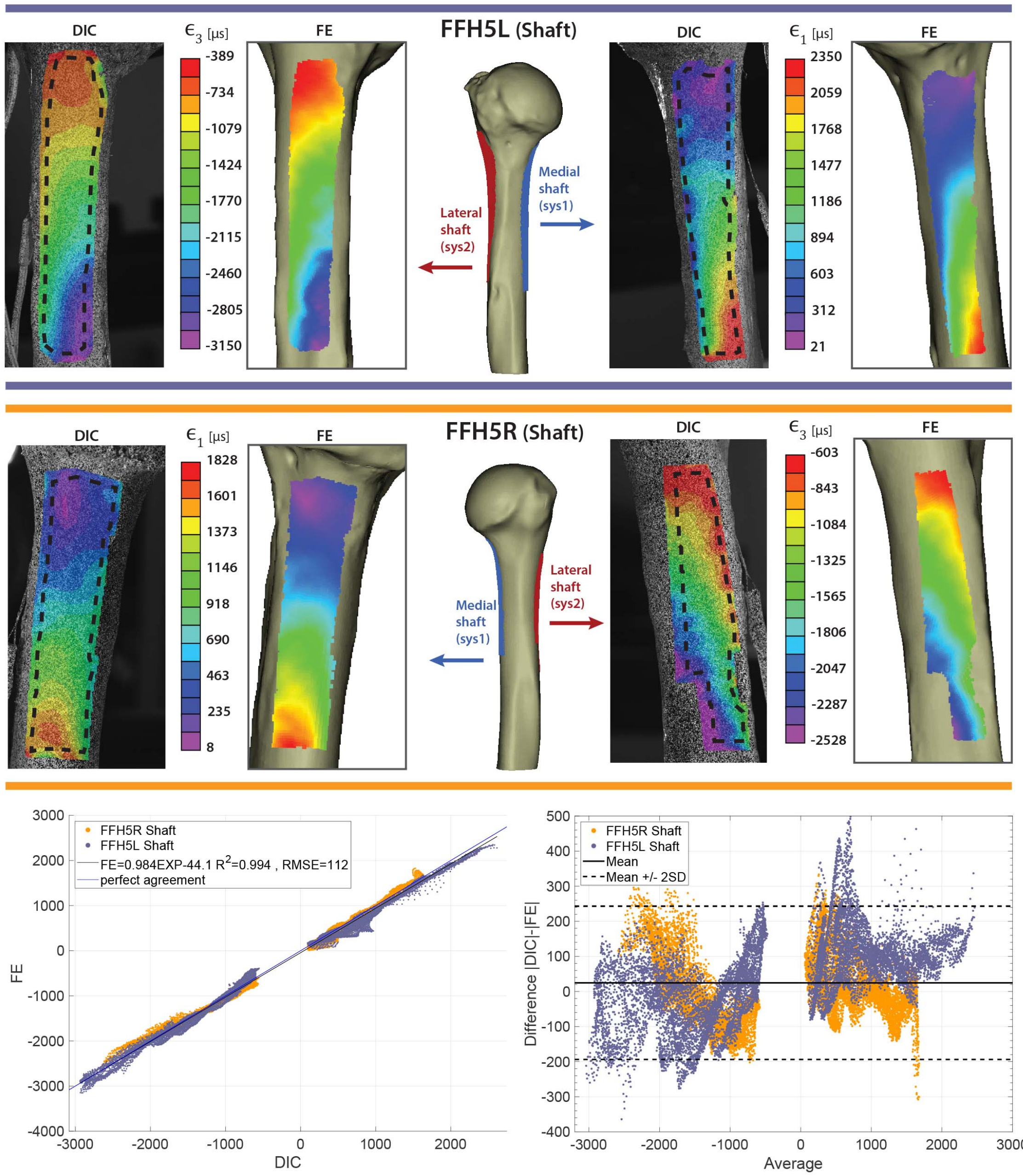

Figure 5: Comparison between DIC and FE principal tension/compression strains in FFH5R and FFH5L shaft.

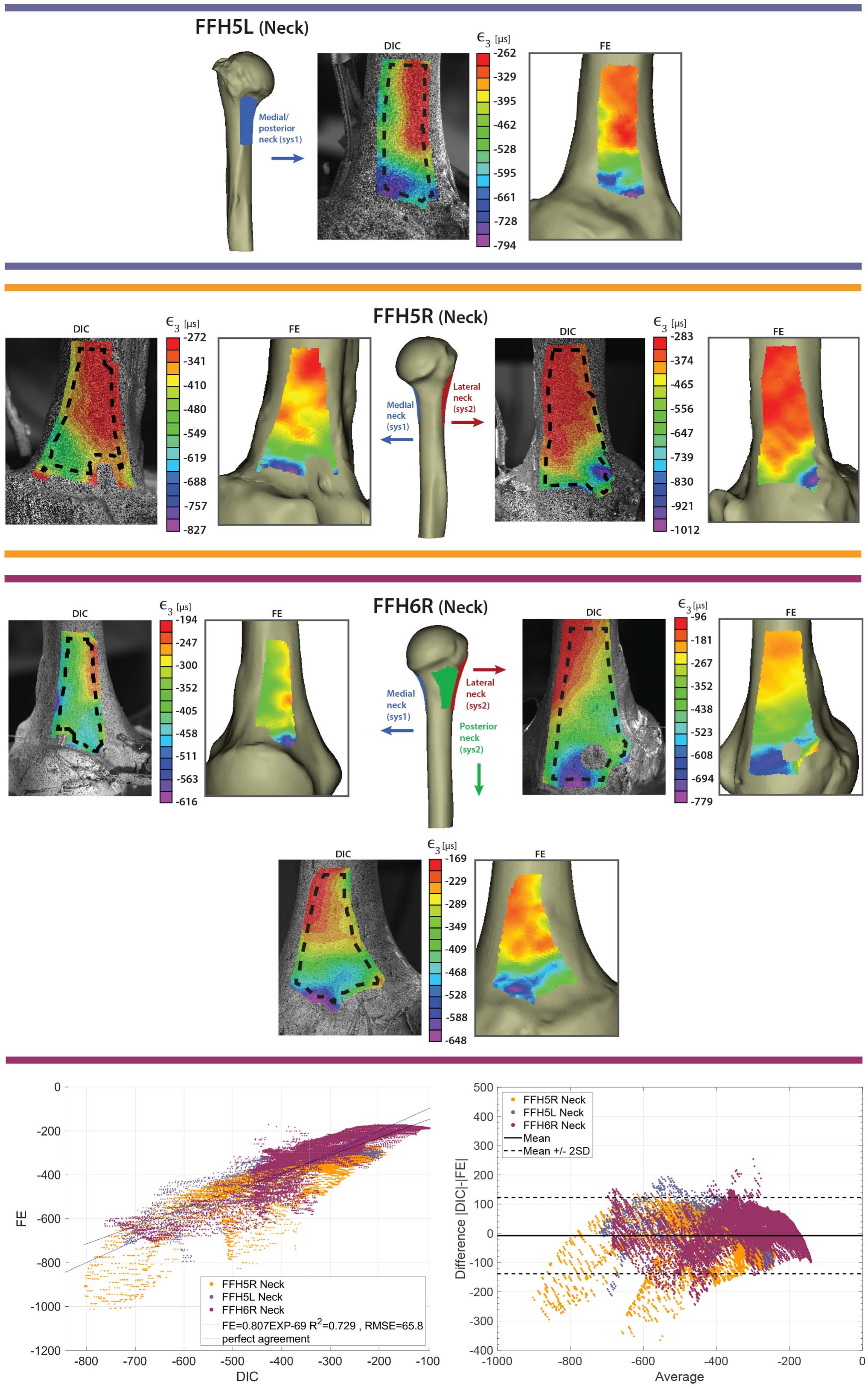

Figure 6: Comparison between DIC and FE principal compression strains in FFH5L, FFH5R and FFH6R neck.

3.2.3. Humeral neck modeling

Implementation of the CBM algorithm resulted in a stiffer model, predicting strains that were too low which had worsened the agreement. The obtained linear slope is 0.48 with R^2 =0.59 (comparing to 0.807 and 0.73 respectively in the standard model, see (11)) and RMSE increased from 66 to 91 μstrain. Using the new $E(\rho)$ relationship, the correlation statistics obtained were almost identical to these of the standard model, with a linear slope of 0.79, R^2 =0.746 and RMSE of 62 μstrain. The cortex width in the surgical neck region is up to 1.5 mm (and mostly around 1 mm).

3.3. Yield loads

A surgical neck fracture was realized in the four humeri in the destructive experiments. According to AO classification [28], this fracture is classified as extra-articular with an impacted metaphyseal (AO/A2). Fractured humeri and typical X-ray scans of the relevant classification are illustrated in Figure 7:Upper.

Force vs. strain closest to fracture location (as recorded by DIC) for FFH5L, FFH5R and FFH6R are shown in Figure 7:Lower. Force-strain curves of the four humeri fractured at anatomical neck (in [8]) are plotted in gray in same graph. Table 2 summarizes experimental and FE yield loads (together with percentage difference) according to cortical and trabecular maximal compression strains (9). Experimental ultimate load is also indicated. The corresponded values for anatomical neck fractures humeri from [8] are also added to the table. Negative difference indicate higher loads in experiment, positive difference indicate higher loads in analysis.

Location of highest principal compression strain in the trabecular and cortical areas as predicted by CTFEAs are presented in Fig. 8.

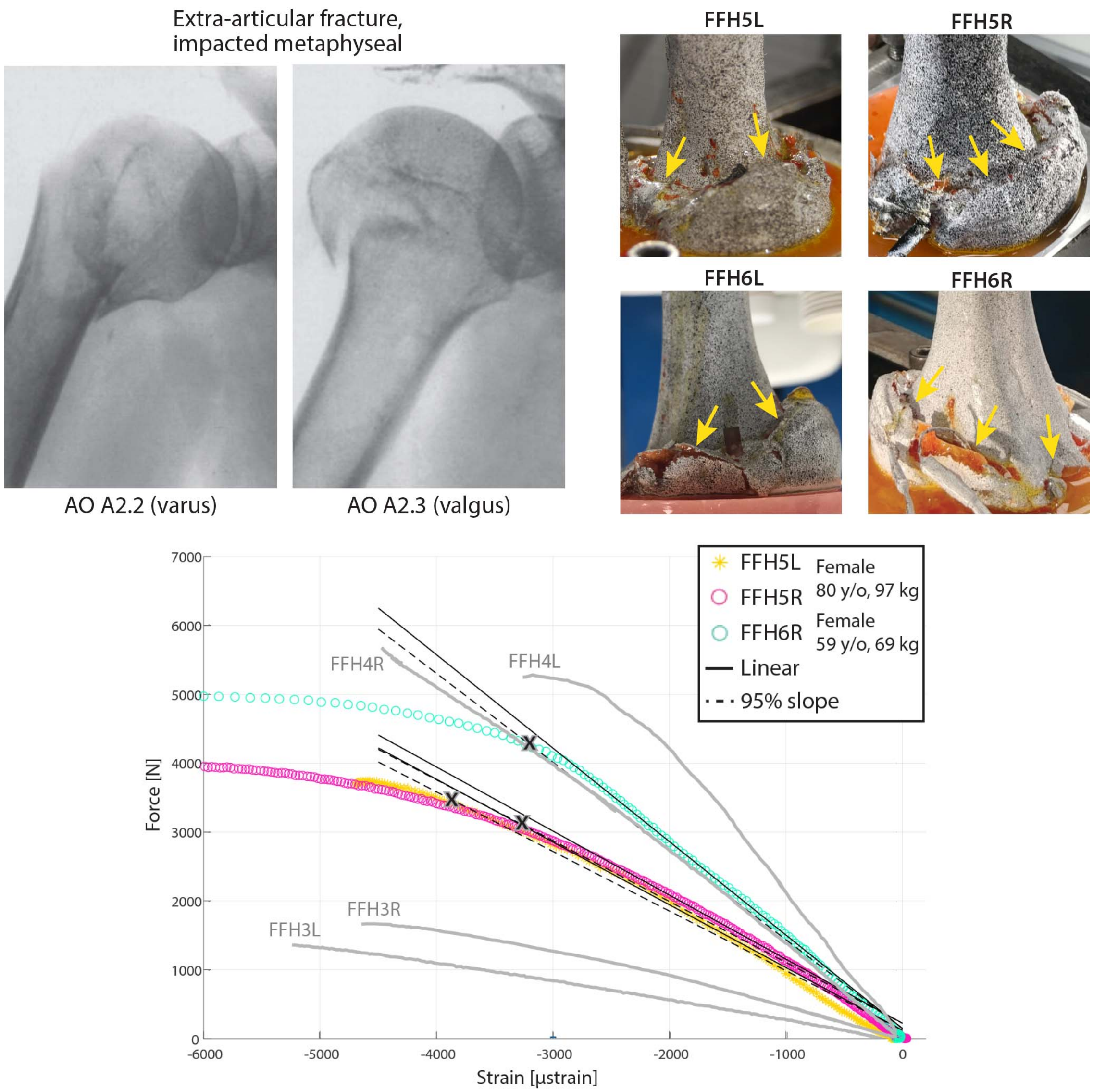

Figure 7: Upper: Fractured humeri showing fracture at their surgical neck, and matching X-rays images (taken from [30]). Lower: Force vs. highest strains measured closest to the fracture location for FFH5R & L and FFH6R. Yield point was defined as the intersection of dashed line (95% of the linear slope) with the force-strain curve. FFH3R & L and FFH4R & L force-strain curves (from [8]) appear in gray.

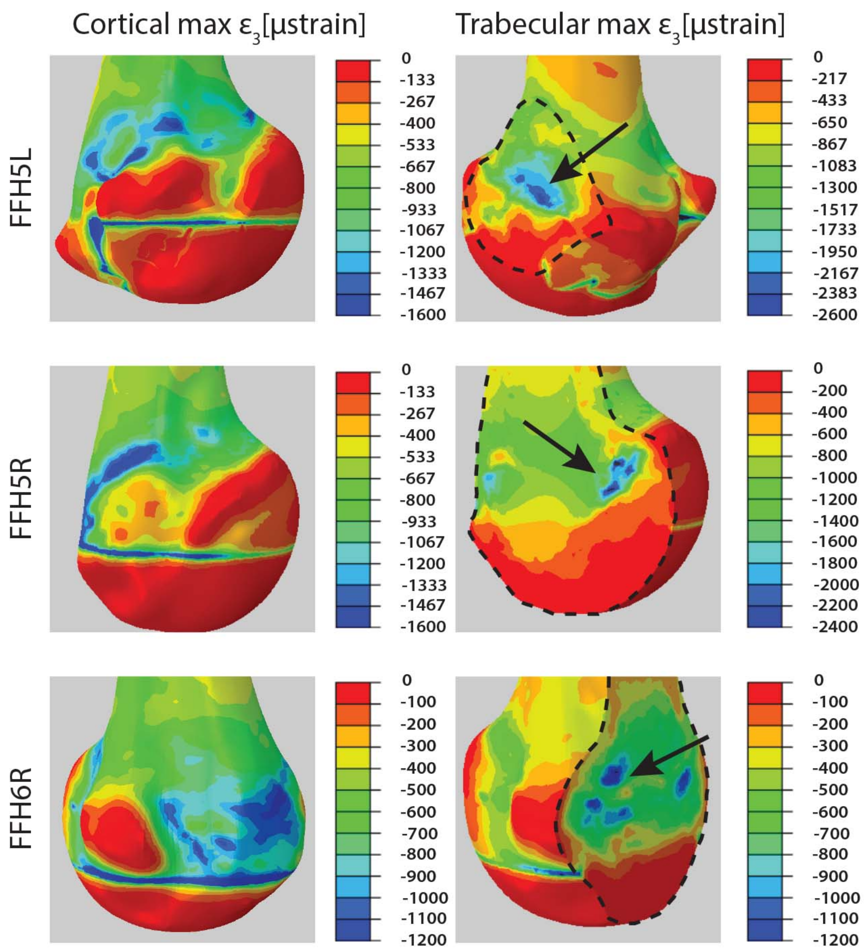

Figure 8: Locations of the predicted maximum value of $|\epsilon_3|$ strain by the CTFEA, obtained in the surgical neck (on bone's surface) and inside the trabecular head/neck.

Table 2: Yield loads based on cortical and trabecular yield criteria from experiments and CTFEA.

Bone label	Exp. yield load [N]	Exp. ult. load [N]	FEA yield load [N]		% Diff.		
			Cortical (-10400μstr.)	Trabecular (-8600μstr.)	Cortical	Trabecular	
FFH3L*	1300	1380	1092	1040	-16	-20	Anatomical neck fractures
FFH3R*	1280	1630	1012	1248	-20.9	-2.5	
FFH4L*	5000	5290	4914	4160	-1.7	-16.8	
FFH4R*	5000	5750	4587	4160	-8.3	-16.8	
FFH5L	3500	3736	5473	4048	56.3	15.7	Surgical neck fractures
FFH5R	3200	3950	5629	4385	75.9	37	
FFH6R	4400	4970	8026	5235	82.4	19	

* Data taken from [8].

4. Discussion

Computing humeri stiffness and strength may be useful in clinical practice, and may enable to predict patients' risk to fracture the bone , thereby *grading* their need for preventive treatment.

The creditability of such FE models for humeri was herein investigated using full field DIC strains and displacements measurements. To the best of our knowledge, this is the first study to document and report FEA validation based on DIC experiments for fresh frozen humeri, and the first experimental setup proposed to in-vitro induce surgical neck fractures. The available literature includes studies considering femoral bones, or humeri studies focusing on comparing different fixations rather than FE models validation [10, 15, 19, 26].

Experiments using DIC were conducted on four humeri imaging both shaft and neck regions. Strains were carefully analyzed and spatially and temporally filtered to reduce noise. These were compared to 12 SGs, with differences less than 10%, thus suggesting that DIC is an appropriate substitute to SGs for strain measurements in humeri experiments. These results are in agreement with SG-DIC comparison made for femurs, also showing high correspondence between the two measurement methods [19].

Displacements recorded by DIC enabled to assess whether proper boundary conditions were applied on FE models, based on which we identified that boundary conditions on FFH6L does not represent the experimental configuration (and thus excluded). For other three humeri (except lateral neck of FFH6R), the experimental and FE agreement in the displacements seemed sufficient, especially in the proximal part of the AOIs where the highest strains were observed (the more relevant region).

Comparing DIC and CTFEA strains, an excellent agreement was obtained on the medial and lateral shafts (FFH5L and FFH5R) with regression slope almost 1 and coefficient of determination > 0.99. At the neck the correlation was fair with regression slope 0.8 and $R^2 = 0.73$. The %RMSE was $\sim$10% on the shaft and $\sim$ 18% at the neck. This outcome is consistent with our former results, when validated by SGs measurements, where it was shown that shaft FE strains are in better agreement with experiments than neck FE strains

[8]. The reason for the substantial differences between the shaft and the neck is probably attributed to inaccurate modeling of the thin cortical shell characterizing the neck regions in long bones. This is supported by the fact that this phenomena was also evident in femoral neck strains, as shown in the studies by [13, 19].

Proper representation of the neck region in FE analyses is attributed to sufficient CT resolution and appropriate modeling of trabecular constitutive model. Our analysis of CBM correction algorithm demonstrated that it may not be appropriate for proximal humeri. The application of CBM to femurs (for which it was originally developed) has shown to improve the agreement of upper neck strains with the experiments, as recently presented in [18]. Differences between the bones may be related to their outer geometry. Femoral neck is shaped like a saddle, such that its outer cortex layer can be *missed* in the scan, which is not the case for the humerus. Since highest HU values are found on bone's boundary, this artifact causes the upper neck of the femur in the model to be "too soft". Bearing this in mind, it seems possible that the *femur-oriented* CBM algorithm may only be appropriate for correcting this specific saddle region of the femur, while in other cases of thin cortices (like in the humerus) it results in an "over-stiff model".

As for the new $E(\rho)$ relationship in the trabecular region, the correlation to experiments is almost indifferent to the examined change, thus the alternative material properties should not be preferred over the original ones.

All tested humeri experienced an impacted fracture of the surgical neck. This fracture pattern is common in clinical practice, consisting of about 18% of all proximal humeri fractures (up to 50% when including these also involving one of the tuberosities [4]).

Yield load predictions based on cortex failure criterion did not represent well the measured ones (three last rows in Table 2). Using the maximum principal compression strain in the trabecular region inside the humerus instead, these were much closer to the experimental ones. This outcome, together with visual inspection of liquids on neck's surface before visible damage, suggests that *impacted fractures initiate inside the humeral head*, causing failure of the trabeculae structure, and thereafter failure extends to outer thin cortex failure. In the humerus this mechanism is apparently unique to impacted fractures, as for anatomical neck fractures (four humeri tested in [8], values in Table 2) yield was predicted with good accuracy (differences smaller than 20%) using the maximum principal compression strain at bone's cortex and conservative predictions were obtained. The different fracture mechanisms are also evident in Figure 7:Lower (colored vs. gray curves), where impacted fractures are characterized by a long "plastic phase" before fracture, as opposed to brittle behavior seen in humeri fractured at the anatomical neck (especially for FFH3L, FFH3R and FFH4R).

Since proximal humeri fractures (and in particular these in the surgical neck) are common in clinical practice, CTFEAs which may predict the fracture risk (via yield load) should be continued to be validated by in-vitro experimental observations which may induce such fractures.

Limitations and future required investigation

Agreement between CTFEA and experimental strains in the neck region and yield loads predictions should be improved. Since some of the discrepancies can be attributed to inaccurate simulation of the experimental BC in the FE models, a different experimental setting fixing the bone's head might have to be used.

Further experiments and CTFEAs, as the ones presented herein, are warrant to enhance the credibility of the CTFEAs.

The dependence of the humerus mechanical response on the trabecular bone inside bone's head and neck is yet to be concluded, simply because the cortex thickness in that region is very small, thus may not dominate the mechanical response properly. It appears that accurate modeling of the orthotropic mechanical response in the trabecular region may be needed to improve the accuracy of the predicted strains, and a more sophisticated nonlinear failure criterion (as the ones proposed for vertebral bodies) may be necessary to predict impacted surgical neck fractures. Since trabecular bone is an highly anisotropic material, the enhancement of CTFEAs to include orthotropic material properties can be a first step in this direction.

References

[1] Altman, D. G., & Bland, J. M. 1983. Measurement in Medicine: The Analysis of Method Comparison Studies Measurement in Medicine: the Analysis of Method Comparison Studiest. *Journal of the Royal Statistical Society. Series D (The Statistician)*, **32**(3), 307–317.

[2] Augat, P., Gordon, C. L., Lang, T. F., Iida, H., & Genant, H.K. 1998. Accuracy of cortical and trabecular bone measurements with peripheral quantitative computed tomography (pQCT). *Physics in Medicine and Biology*, **43**(10), 2873–2883.

[3] Bayraktar, H. H., Morgan, E. F., Niebur, G. L., Morris, G. E., Wong, E. K., & Keaveny, T. M. 2004. Comparison of the elastic and yield properties of human femoral trabecular and cortical bone tissue. *Journal of Biomechanics*, **37**(1), 27–35.

[4] Bergdahl, C., Ekholm, C., Wennergren, D., Nilsson, F., & Möller, M. 2016. Epidemiology and patho-anatomical pattern of 2,011 humeral fractures: data from the Swedish Fracture Register. *BMC Musculoskeletal Disorders*, **17**(1), 159.

[5] Bergmann, G., Graichen, F., Bender, A., Rohlmann, A., Halder, A., Beier, A., & Westerhoff, P. 2011. In vivo gleno-humeral joint loads during forward flexion and abduction. *Journal of Biomechanics*, **44**(8), 1543–52.

[6] Chandran, V., Maquer, G., Gerig, T., Zysset, P., & Reyes, M. 2019. Supervised learning for bone shape and cortical thickness estimation from CT images for finite element analysis. *Medical Image Analysis*, **52**, 42–55.

[7] Court-Brown, C. M., Garg, A., & McQueen, M. M. 2001. The epidemiology of proximal humeral fractures. *Acta Orthopaedica*, **72**(4), 365–371.

[8] Dahan, G., Trabelsi, N., Safran, O., & Yosibash, Z. 2019. Finite element analyses for predicting anatomical neck fractures in the proximal humerus. *Clinical Biomechanics*, **68**, 114–121.

[9] Damm, T., A. Peña, J., Campbell, G.M., Bastgen, J., Barkmann, R., & Glüer, C. 2019. Improved accuracy in the assessment of vertebral cortical thickness by quantitative computed tomography using the Iterative Convolution OptimizatioN (ICON) method. *Bone*, **120**, 194–203.

[10] Dickinson, A. S., Taylor, A. C., Ozturk, H., & Browne, M. 2011. Experimental validation of a finite element model of the proximal femur using digital image correlation and a composite bone model. *Journal of Biomechanical Engineering*, **133**(1), 1–6.

[11] Fankhauser, F., Schippinger, G., Weber, K., Heinz, S., Quehenberger, F., Boldin, C., Bratschitsch, G., Szyszkowitz, R., Georg, L., & Friedrich, A. 2003. Cadaveric-biomechanical evaluation of bone-implant construct of proximal humerus fractures (Neer type 3). *Journal of Trauma*, **55**(2), 345–9.

[12] Goodsitt, M. M. 1992. Conversion relations for quantitative CT bone mineral densities measured with solid and liquid calibration standards. *Bone and Mineral*, **19**(2), 145–158.

[13] Grassi, L., Schileo, E., Taddei, F., Zani, L., Juszczyk, M., Cristofolini, L., & Viceconti, M. 2012. Accuracy of finite element predictions in sideways load configurations for the proximal human femur. *Journal of Biomechanics*, **45**(2), 394–399.

[14] Grassi, L., Väänänen, S. P., Yavari, S. A., Jurvelin, J. S., Weinans, H., Ristinmaa, M., Zadpoor, A. A., & Isaksson, H. 2014. Full-field strain measurement during mechanical testing of the human femur at physiologically relevant strain rates. *Journal of Biomechanical Engineering*, **136**(11), 1–8.

[15] Grassi, L., Väänänen, S. P., Ristinmaa, M., Jurvelin, J. S., & Isaksson, H. 2016. How accurately can subject-specific finite element models predict strains and strength of human femora? Investigation using full-field measurements. *Journal of Biomechanics*, **49**(5), 802–806.

[16] Hangartner, T. N., & Gilsanz, V. 1996. Evaluation of cortical bone by computed tomography. *Journal of Bone and Mineral Research*, **11**(10), 1518–1525.

[17] Kaneko, T. S., Pejcic, M. R., Tehranzadeh, J., & Keyak, J. H. 2003. Relationships between material properties and CT scan data of cortical bone with and without metastatic lesions. *Medical Engineering & Physics*, **25**(6), 445–454.

[18] Katz, Y. 2020. *The mechanical response of a femur with an implant*. PhD thesis, Tel Aviv university.

[19] Katz, Y., & Yosibash, Z. 2020. New insights on the proximal femur biomechanics using Digital Image Correlation. *Journal of Biomechanics*, **101**, 109599.

[20] Katz, Y., Lubovsky, O., & Yosibash, Z. 2018. Clinical Biomechanics Patient-specific finite element analysis of femurs with cemented hip implants. *Clinical Biomechanics*, **58**, 74–89.

[21] Katz, Y., Dahan, G., Sosna, J., Shelef, I., Cherniavsky, E., & Yosibash, Z. 2019. Scanner influence on the mechanical response of QCT-based finite element analysis of long bones. *Journal of Biomechanics*, **86**, 149–159.

[22] Keller, T. S. 1994. Predicting the compressive mechanical behavior of bone. *Journal of Biomechanics*, **27**(9), 1159–1168.

[23] Keyak, J. H., Lee, I. Y., & Skinner, H. B. 1994. Correlations between orthogonal mechanical properties and density of trabecular bone: Use of different densitometric measures. *Biomedical Materials*, **28**, 1329–1336.

[24] Keyak, J. H., Kaneko, T. S., Tehranzadeh, J., & Skinner, H. B. 2005. Predicting proximal femoral strength using structural engineering models. *Clinical Orthopaedics and Related Research*, **437**, 219–228.

[25] Kim, S. H., Szabo, R. M., & Marder, R. A. 2012. Epidemiology of humerus fractures in the United States: Nationwide emergency department sample, 2008. *Arthritis Care and Research*, **64**(3), 407–414.

[26] Mathison, C., Chaudhary, R., Beaupre, L., Reynolds, M., Adeeb, S., & Bouliane, M. 2010. Biomechanical analysis of proximal humeral fixation using locking plate fixation with an intramedullary fibular allograft. *Clinical Biomechanics*, **25**(7), 642–646.

[27] Mindways Software Inc. 2002. *CT Calibration Phantom Users Guide*. Tech. rept. Austin, TX, USA.

[28] Muller, M.E., S., Nazarian, Koch, P., & Schatzker, J. 1990. *The comprehensive classification of fractures of long bones*. Berlin: Springer-Verlag.

[29] Museyko, O., Gerner, B., & Engelke, K. 2017. A new method to determine cortical bone thickness in CT images using a hybrid approach of parametric profile representation and local adaptive thresholds: Accuracy results. *PLOS ONE*, **12**(11), e0187097.

[30] Orozco, R., Sales, J.M., & Videla, M. 2000. *Atlas of Internal Fixation*. Berlin: Springer-Verlag.

[31] Prevrhal, S., Engelke, K., & Kalender, W. A. 1999. Accuracy limits for the determination of cortical width and density: The influence of object size and CT imaging parameters. *Physics in Medicine and Biology*, **44**(3), 751–764.

[32] Prevrhal, S., Fox, J. C., Shepherd, J. A., & Genant, H. K. 2003. Accuracy of CT-based thickness measurement of thin structures: Modeling of limited spatial resolution in all three dimensions. *Medical Physics*, **30**(1), 1–8.

[33] Schileo, E., Dall'Ara, E., Taddei, F., Malandrino, A., Schotkamp, T., Baleani, M., & Viceconti, M. 2008a. An accurate estimation of bone density improves the accuracy of subject-specific finite element models. *Journal of Biomechanics*, **41**(11), 2483–2491.

[34] Schileo, E., Taddei, F., Cristofolini, L., & Viceconti, M. 2008b. Subject-specific finite element models implementing a maximum principal strain criterion are able to estimate failure risk and fracture location on human femurs tested in vitro. *Journal of Biomechanics*, **41**(2), 356–367.

[35] Schileo, E., Pitocchi, J., Falcinelli, C., & Taddei, F. 2020. Cortical bone mapping improves finite element strain prediction accuracy at the proximal femur. *Bone*, **136**, 115348.

[36] Skedros, J. G., Knight, A. N., Pitts, T. C., O'Rourke, P. J., & Burkhead, W. Z. 2016. Radiographic morphometry and densitometry predict strength of cadaveric proximal humeri more reliably than age and DXA scan density. *Journal of Orthopaedic Research*, **34**(2), 331–341.

[37] Trabelsi, N., Yosibash, Z., Wutte, C., Augat, P., & Eberle, S. 2011. Patient-specific finite element analysis of the human femur-A double-blinded biomechanical validation. *Journal of Biomechanics*, **44**(9), 1666–1672.

[38] Treece, G. M., & Gee, A. H. 2015. Independent measurement of femoral cortical thickness and cortical bone density using clinical CT. *Medical Image Analysis*, **20**(1), 249–264.

[39] Treece, G. M., Gee, A. H., Mayhew, P. M., & Poole, K. E.S. 2010. High resolution cortical bone thickness measurement from clinical CT data. *Medical Image Analysis*, **14**(3), 276–290.

[40] Treece, G. M., Poole, K. E.S., & Gee, A. H. 2012. Imaging the femoral cortex: Thickness, density and mass from clinical CT. *Medical Image Analysis*, **16**(5), 952–965.

[41] van Eck, C. F., Klein, C. M., Rahmi, H., Scheidt, K. B., Schultzel, M., Lee, B. K., & Itamura, J. M. 2019. Morbidity, mortality and cost of osteoporotic fractures—should proximal humerus fractures be taken as seriously as hip fractures? *Annals of Joint*, **4**.

[42] Yosibash, Z., Trabelsi, N., & Milgrom, C. 2007. Reliable simulations of the human proximal femur by high-order finite element analysis validated by experimental observations. *Journal of Biomechanics*, **40**(16), 3688–3699.

[43] Yosibash, Z., Tal, D., & Trabelsi, N. 2010. Predicting the yield of the proximal femur using high-order finite-element analysis with inhomogeneous orthotropic material properties. *Philosophical Transactions of the Royal Society A*, **368**(1920), 2707–2723.

[44] Yosibash, Z., Plitman Mayo, R., Dahan, G., Trabelsi, N., Amir, G., & Milgrom, C. 2014. Predicting the stiffness and strength of human femurs with real metastatic tumors. *Bone*, **69**, 180–190.